Soft Matter

Tiling patterns from ABC star molecules: 3-colored foams?

Journal:	*Soft Matter*
Manuscript ID:	SM-ART-05-2014-001052.R1
Article Type:	Paper
Date Submitted by the Author:	21-Jun-2014
Complete List of Authors:	Kirkensgaard, Jacob; University of Copenhagen, Niels Bohr Institute Pedersen, Martin; University of Copenhagen, Niels Bohr Institute Hyde, S; R.S. Phys. S., Applied Mathematics Department

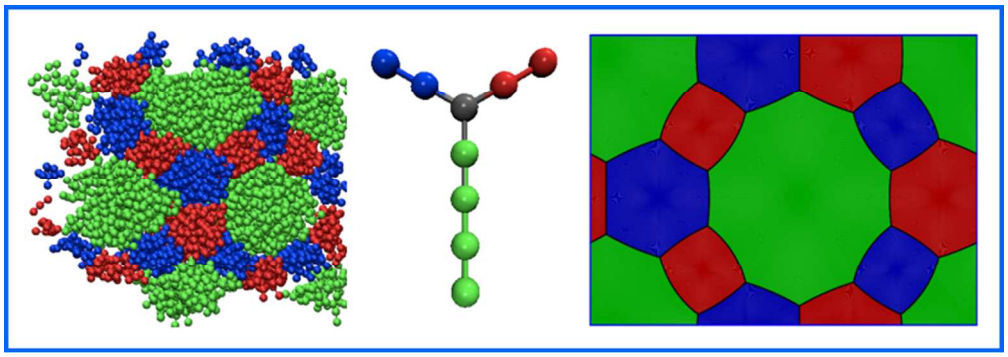

Based on coarse-grained simulations and Surface Evolver calculations we explore if the formation of tiling patterns formed by ABC star molecules can be considered 3-colored foams.

ARTICLE TYPE www. rsc.org/xxxxxx | XXXXXXXX

Tiling patterns from ABC star molecules: 3-colored foams?†

Jacob J. K. Kirkensgaard,*[a] Martin C. Pedersen,[a] and Stephen T. Hyde[a,b]

Received Xth XXXXXXXXXX 20XX, Accepted Xth XXXXXXXXX 20XX
First published on the web Xth XXXXXXXXXX 200X
DOI: 10.1039/b000000x

We present coarse-grained simulations of the self-assembly of 3-armed ABC *star polyphiles*. In systems of star polyphiles with two arms of equal length the simulations corroborate and expand previous findings from related miktoarm star terpolymer systems on the formation of patterns containing columnar domains whose sections are 2D planar tilings. However, the systematic variation of face topologies as the length of the third (unequal) arm is varied differs from earlier findings regarding the compositional dependence. We explore 2D 3-colored foams to establish the optimal patterns based on interfacial energy alone. A generic construction algorithm is described that accounts for all observed 2D tiling patterns and suggests other patterns likely to be found beyond the range of the simulations reported here. Patterns resulting from this algorithm are relaxed using *Surface Evolver* calculations to form 2D foams with minimal interfacial length as a function of composition. This allows us to estimate the interfacial enthalpic contributions to the free energy of related star molecular assemblies assuming strong segregation. We compare the resulting phase sequence with a number of theoretical results from particle-based simulations and field theory, allowing us to tease out relative enthalpic and entropic contributions as a function of the chain lengths making up the star molecules. Our results indicate that a richer polymorphism is to be expected in systems not dominated by chain entropy. Further, analysis of corresponding planar tiling patterns suggests that related two-periodic columnar structures are unlikely hypothetical phases in 4-arm star polyphile melts in the absence of sufficient arm configurational freedom for minor domains to form lens-shaped di-gons, which require higher molecular weight polymeric arms. Finally, we discuss the possibility of forming a complex tiling pattern that is a quasi-crystalline approximant for 3-arm star polyphiles with unequal arm lengths.

1 Introduction

Considerable attention has recently been devoted to the exploration of micro-phase separated structures in melts of star-shaped ABC miktoarm copolymers with a number of reports of synthesis, experiments and theory[1–24]. So far focus has been principally directed towards segregated cylindrical mesostructural self-assemblies, whose orthogonal sections are two-dimensional (2D) 3-colored tiling patterns of the plane. More recently an exploration of the self-assembly of lower molecular weight analogues of ABC miktoarm copolymers, termed 'star polyphiles', has been initiated[25–28]. Star polyphiles are oligomers rather than polymers, current examples contain hydrophilic, oleophilic and fluorophilic oligomeric chains attached to a common central junction. These molecules resemble amphiphiles, in that they can self-assemble in solution, with an additional fluorocarbon moiety that is designed to be immiscible with the other two moieties. As with miktoarm star terpolymers, this extra arm induces novel topological constraints on the hydrophilic, oleophilic and fluorophilic micro-domains. Scattering experiments and polarised optical microscopy confirm the possibility of self-assembly of three-arm star polyphiles into a number of distinct liquid crystalline mesophases. A relevant example in this context is the formation of a [12.6.4] tiling pattern[27], so far the only experimental report on liquid crystalline structure formation in these novel molecular systems. However, star polyphiles could very likely mimic the behavior of miktoarm copolymers in the same way that amphiphiles and diblock copolymers display a number of common mesophases despite differences in size and underlying segregation mechanisms. The simulations presented below indicates that this is indeed the case.

Previous simulations by Dotera and colleagues have established the possibility of a number of mesostructures whose cross-sections are various planar tilings, including several patterns already observed in actual miktoarm copolymer systems. These include most Archimedean tilings[13,14,29] as well as quasi-crystalline patterns[30]. Their investigations used a lattice Monte Carlo (MC) approach. Huang *et al.* and Kirkensgaard have implemented dissipative particle dynamics (DPD) simulations to explore miktoarm copolymer self-assembly as

† Electronic Supplementary Information (ESI) available: [Additional simulation details, example *Surface Evolver* batch script, barycentric embeddings of tiling patterns]. See DOI: 10.1039/b000000x/

[a] *Niels Bohr Institute, University of Copenhagen, Denmark; E-mail: jjkk@nbi.dk*
[b] *Applied Mathematics, Research School of Physical Sciences, Australian National University, Canberra, Australia*

a function of the interactions between the molecular species, the molecular architecture and from blending different block copolymers[15,21–24,31]. The DPD simulations are generally consistent with the Monte Carlo simulations of Dotera *et al.* The self-assembly of ABC miktoarm star terpolymers has also been addressed using self-consistent field theory (SCFT) in various implementations (real vs. reciprocal space and 2D vs 3D based)[17–20]. The SCFT predictions are qualitatively in line with the simulations mentioned above although slight variations in the compositional dependence are found, also between the different SCFT studies. In this paper we compare and contrast simulations of self-assembly of star polyphiles with the simulation and field theory calculations of miktoarm copolymers.

Our simulations described below employ harder Lennard-Jones based interaction potentials compared to the DPD, MC and SCFT work described above. This is to mimic the short chain nature of the polyphile molecules compared to for example the DPD method where very soft potentials are typically used to describe polymers. Our simulations are a kin to recent work on bola-amphiphiles which also show related supramolecular structure formation[32,33]. As described below the differences in the theoretical methods lead to differences in the progression of tilings patterns as a function of composition. This leads us to the question of whether the formation of these structures are primarily a result of interfacial energy minimization, i.e. whether the tilings can be described as 3-colored foams, or to what extent the chain nature of the molecules determine the resulting assemblies. As is well known from both amphiphilic and block copolymer self-assembly, the formation of complex morphologies is a result of a delicate free energy balance between enthalpic and entropic (packing related) contributions. To test this hypothesis we propose a generic algorithm to generate relevant tiling patterns which we use as input for *Surface Evolver* calculations. The *Surface Evolver* employ an area-minimizing algorithm to determine the optimal pattern as a function of composition based on interfacial energy alone, i.e. treating the structures as 3-colored foams. This allows us to completely separate out the interfacial enthalpic contribution and we compare and discuss the results in light of the simulations and the above mentioned results from the literature.

2 Simulation details

We employ a simple coarse-grained approach to simulate self-assembly of star polyphiles into mesoscale structures[25]. The simulation technique is an extension of a setup originally developed specifically to model assembly of lipid bilayers[34–36]. The original model reduced lipid molecules to linked beads of two 'colors' representing hydrophobic and hydrophilic moieties respectively. In our modified model, shown in Figure 1, each molecule consists of a neutral junction bead and an (in principle) arbitrary number of arms attached, in this case three. Each (A,B and C) arm has a single color (red, blue and green respectively), distinct from those of the other arms. Self-assembly is driven by effective attractions between like arms of different molecules as described below.

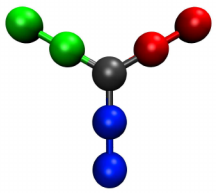

Fig. 1 Rendering of the model star molecule. A neutral center junction connects 3 mutually immiscible arms, indicated by different colors: A (red), B (blue) and C (green). Here $x = 1$, the ratio of C to A length.

Molecular dynamics (MD) simulations are performed using a modified version of the *mbtools* extension to the *Espresso* package[37]. The simulations presented employ the following interactions: all bead sizes are controlled via a repulsive truncated and shifted Lennard-Jones potential

$$V_{\text{rep}}(r,b) = \begin{cases} 4\varepsilon\left[\left(\frac{b}{r}\right)^{12} - \left(\frac{b}{r}\right)^{6} + \frac{1}{4}\right] & \text{for } r \le r_c \\ 0 & \text{for } r > r_c \end{cases} \quad (1)$$

where ε and σ denote our units of energy and length respectively. The cut-off distance, $r_c = 2^{1/6}b$ where b is the bead diameter. Connected beads along each arm are linked by a Finite Extensible Nonlinear Elastic (FENE) bond

$$V_{\text{bond}} = -\frac{1}{2}k_{\text{bond}}r_\infty^2 \log[1-(r/r_\infty)^2] \quad (2)$$

with stiffness $k_{\text{bond}} = 30\varepsilon/\sigma^2$ and divergence length $r_\infty = 1.5\sigma$. We impose a harmonic spring potential between the central junction bead and the terminal bead of each arm, tending to straighten the arms.

$$V_{\text{bend}} = \frac{1}{2}k_{\text{bend}}(r - l_c\sigma)^2. \quad (3)$$

where the bending stiffness $k_{\text{bend}} = 0.5\varepsilon/\sigma^2$ and $l_c = n_b + 2$, n_b being the number of beads of the arm in question. Lastly, an attractive potential acts between all beads of same color (i.e. between like arms) according to the function:

$$V_{\text{attr}}(r,b) = \begin{cases} -\varepsilon & \text{for } r < r_c \\ -\varepsilon\cos^2\left[\frac{\pi(r-r_c)}{2w_c}\right] & \text{for } r_c \le r \le r_c + w_c \\ 0 & \text{for } r > r_c + w_c \end{cases} \quad (4)$$

This potential has attractive depth ε and an interaction range set by the distance scale parameter w_c. As described previously values of w_c around 1.2 - 1.6 σ is found to be optimal for these simulations[25]. All simulations presented were run with equivalent attractive interactions between all like beads and $\sigma = 1$, $\varepsilon = 1$. They were performed as constant volume (NVT ensemble) simulations using a Langevin thermostat at temperature $k_BT = 1.5\varepsilon$ and with time steps $\delta t = 0.01\tau$ and a friction constant $\Gamma = \tau^{-1}$ (in units of Lennard-Jones time τ). A cubic box of side length L with period boundary conditions constrained the ensemble. All simulations were started from a random gas configuration and run until an equilibrium state was reached, which is usually easily determined visually. Additional details of the different simulations are given in the Supplementary Information. Simulation snapsnots were all made with the VMD package[38].

3 Self-assembly of $1:1:x$ polyphiles

We analyzed first the effect of varying the length of one (green) arm while fixing the other (red and blue) arm lengths to be equal. We quantify the composition by the parameter x defined as the ratio of C to A beads, eg. $x = 2$ means that the green C arm is twice as long as the red A and blue B arms. Various bead numbers were used in the coarse-graining, to allow variation of the relative lengths. A number of distinct mesophases were detected, depending on x. These are summarized visually in Figure 2.

Lamellar phase

When one of the arms is significantly shorter than the other two (i.e. x is small) the system self-assembles to a lamellar phase. This is not surprising, since in the limit of vanishing x, the star polyphile reverts to a conventional amphiphile, with equivalent hydrophobic and hydrophilic domain volumes. We find that the minority component is distributed uniformly over the whole interface, consistent with the copolymer simulations[15]; however we do not find spherical domains, as reported elsewhere[13]. This polyphile mesostructure is that expected from self-consistent field theory (SCFT)[17] as also remarked by others[15]. However, while this result is attributed to the segregation level (strong vs. weak) in the case of copolymeric molecules, our smaller molecules aggregate to give a uniform distribution of the extremely short green chains for entropic reasons alone.

Bicontinuous Double Diamond phase

For slightly longer green chains, the system adopts a novel multicontinuous morphology, previously unreported. The two larger red and blue components form a pair of equivalent interwoven labyrinths whose channels lie on diamond networks. The minority component and junction region form a sponge-like pattern closely resembling the triply-periodic D minimal surface, separating the two labyrinths. The resulting pattern is a cubic mesophase with space group symmetry $Fd\bar{3}m$.

For still larger green arms, a variety of columnar phases result, discussed below. The star polyphiles thus effect a transition from a lamellar phase to columnar phases via a bicontinuous phase, as expected from geometric considerations of amphiphilic systems if the amphiphile has an effective taper in cross-sectional area from the hydrophobic-hydrophilic interface to the free hydrophobic chain ends[39]. For our 3-arm star polyphiles, the reasonably small green arms ($x \sim 0.2$), effectively mix with both the red and blue domains, forming swollen regions between the red and blue domains, thereby mimicking the molecular shape of a tapered amphiphilic bilayer (with red and blue monolayers, glued by the green intermediate domain).

Harlequin pattern

Still further green arm growth leads to a novel intermediate mesophase, where the green minority component uniformly lines the red-blue interfaces forming flat walls, as well as forming small cylindrical domains. The intermediate cylindrical phase resembles a 'harlequin' pattern, of alternating blue and red columns whose sections are distorted octagons. Adjacent like-coloured red and blue domains are separated by quadrilateral prismatic green domains, adjacent domains of distinct colours by green walls. This harlequin phase is only found for x = 0.25 but is stable over long simulation times. It has not been reported previously.

Tiling patterns

For $x > 0.33$ the smaller green component forms distinct prismatic domains, rather than walls between the two bulkier red and blue domains detected at lower x. Assemblies of the 3-arm star polyphiles thus segregate into 3 distinct phases, that meet along three-phase "triple-lines". For still larger green arms, a suite of columnar mesophases are formed, whose 2D sections are planar tiling patterns. We describe these patterns by a 2D Schläfli symbol $[k_1.k_2.k_3]$, describing the polygons (of size k_1, k_2 and k_3) common to each vertex (see caption to Figure 2).

When the relative volume fraction of the green arms, $x \sim 0.33 - 0.5$, a rectangular [8.8.4] pattern is formed. The balanced case, for which all three arms are roughly equal in size,

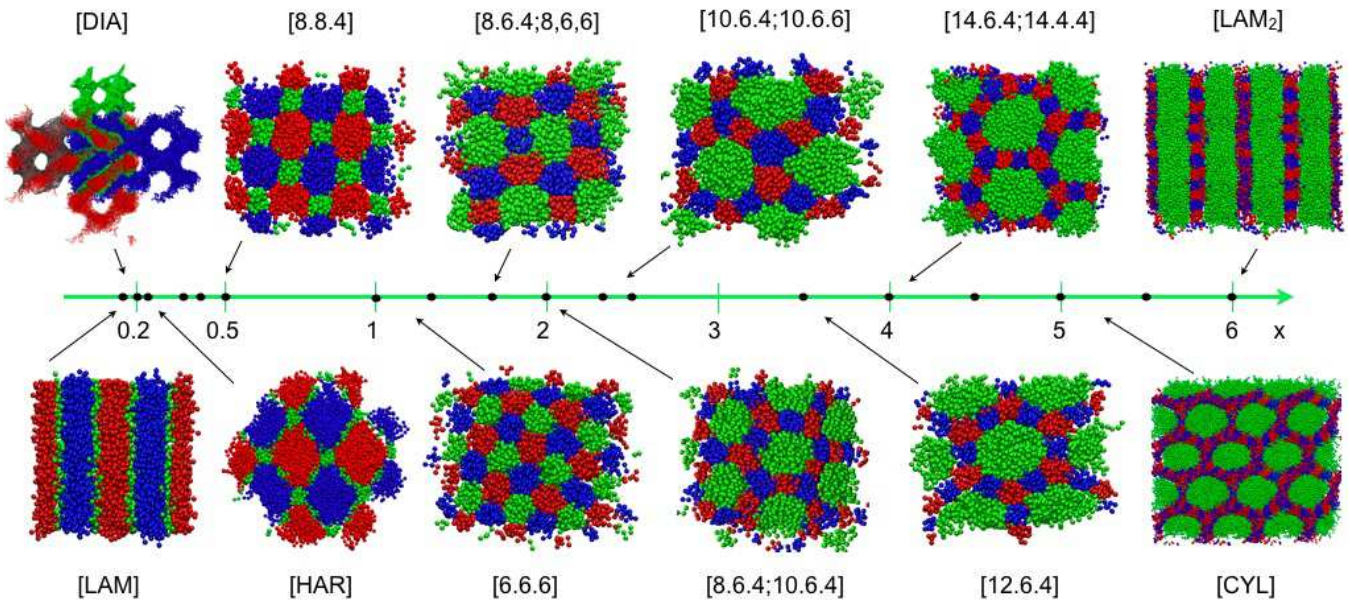

Fig. 2 Phase diagram of model star polyphiles when varying the length of one arm while keeping the others fixed at equal (unit) length. The parameter x is the fractional length of the green domain in all snapshots. The different tiling patterns are named by their Schläfli symbol [13] that assigns a polygonal tiling pattern a set of numbers $[k_1.k_2.....k_l]$ indicating that a vertex in the tiling is surrounded by a k_1-gon, a k_2-gon, ... in cyclic order. Tilings with more than one topologically distinct vertex are denoted $[k_1.k_2.k_3;k_4.k_5.k_6]$. The black dots along the x-axis indicates the precise location of the discrete bead number variation. See Table S1 for details.

($x \sim 1$) gives the Platonic hexagonal honeycomb, whose section is the [6.6.6] tiling, resulting in a hexagonal columnar mesophase. If the green arms occupies slightly more volume than the equal red and blue arms, i.e. $x \sim 1.75$ a columnar phase with square, hexagonal and octagonal columns was found. The associated 2D tiling has topology [8.6.4;8.6.6], with two topologically distinct vertices. For $x \sim 2-3$, the simulations are generally more difficult to equilibrate, in agreement with Dotera *et al*. However, a columnar phase whose 2D section is the [8.6.4;10.6.4] tiling has been observed. As the relative volume of the green arm grows larger still, four further columnar phases are found. We describe these patterns by their 2D sections: the [10.6.4;10.6.6] tiling, the [12.6.4] Archimedean tiling, the [14.6.4;14.4.4] tiling and a cylindrical phase denoted [CYL]. There are elements of 16- and 18-gons in the three [CYL] patterns but no conclusive results have been produced, partly because the equilibration of these rather large molecules is computationally very demanding in the present setup. However, as discussed below we have good reason to believe that [16.6.4;16.4.4] and/or [18.6.4;18.4.4] tilings could be found in these systems. Among the observed tiling patterns, those containing [8.6.4;10.6.4] and [14.6.4;14.4.4] planar sections are novel compared to the polymer simulations mentioned above [13,15,21].

Hierarchical lamellae

Lastly, at $x = 6$ a hierarchical lamellar phase forms in preference to a columnar topology. Here the green majority component forms a lamellar phase, separated by red and blue domains which themselves build distinct lamellar phases, orthogonal to the green lamellae. (In our simulation the neighboring red-blue domains on either side of the green domain is rotated 45 degrees relative to each other which is why the central red-blue region looks disordered in the figure.) A similar structure was found previously [13], both with and without relative rotations of the minority domains.

4 Generation of potential patterns consistent with the 3-arm star molecular architecture

The formation of prismatic patterns based on a limited subset of possible two-dimensional tilings of the plane in $1:1:x$ ABC star systems can be understood by taking note of the following requirements imposed by these star molecules. First, all tilings must contain only vertices of degree-three, consistent with the molecules' three-arm topology. Second, in order to allow a 3-coloured pattern, all tiles must be bounded by polygons with an even number of sides [13]. To see why, consider the dual 2D graph, whose vertices, edges and faces are

formed by the faces, edges and vertices respectively of the original 2D tiling. We require each vertex to be coloured red, green or blue, and all vertices sharing an edge to be coloured differently. Consider the wheel of vertices, all connected to a central (green, say) vertex by spoke-like edges (fig. 3); evidently, these wheel vertices must be alternately coloured red and blue. To avoid like-coloured adjacent vertices, the wheel must contain an even number of vertices, so the number of spokes radiating from the (arbitrary) vertex (equal to the degree of the vertex) must be even. Since the vertex degree of the dual is equal to the polygonal size of the original graph, all relevant 2D tilings must contain even-sided polygons only. Third, since the molecules have composition red:blue:green

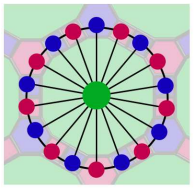

Fig. 3 Wheel construction (bold black lines and coloured vertices) of dual graph to 3-coloured tiling (faint coloured tiling in background). All the vertices of the dual graph linked to a common central (green) hub vertex must alternate between red and blue, hence the number of spokes radiating from the hub must be even.

= 1:1:x, the areas of two of the three polygons (gauged by their in-circle or out-circle radii) around each vertex should be roughly equal.

For simplicity, assume for now that all vertices are topologically equivalent, so the tiling has Schläfli symbol $[n_R.n_G.n_B]$. Euler's relation for degree-3 tilings constrains the polygons n_R, n_G and n_B about each vertex as follows:

$$V - E + F = 2 \tag{5}$$

For each vertex then, the tiling contains $\frac{3}{2}$ edges (since it is of degree-three), and $\frac{1}{n_i}$ faces for each of the three (n_i-sided) polygons incident to that vertex. i.e.:

$$1 - \frac{E}{V} + \frac{F}{V} = 1 - \frac{3}{2} + \frac{1}{n_R} + \frac{1}{n_G} + \frac{1}{n_B} = \frac{2}{V} = 0, \tag{6}$$

since the number of vertices is unbounded ($V = \infty$). Therefore,

$$n_R n_G n_B = 2(n_G n_B + n_R n_B + n_G n_R) \tag{7}$$

Suppose first that the smallest (e.g. green) polygons are di-gons – lenses. In that case, no planar tessellations are possible under the constraint of eq. 7 since it has no pair of positive integer solutions for n_R and n_B when $n_G = 2$. However, we can form an infinite variety of topologically admissible patterns containing green digons, red polygons of arbitrary size and multiply-connected blue domains as follows. First, form 'necklaces' of di-gons, then scatter these in the plane so that they do not intersect, e.g. fig. 4. The resulting 3D patterns are disordered arrays of red cylinders, decorated by smaller green cylinders, embedded in a continuum of blue.

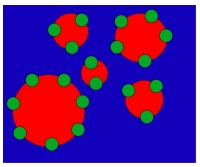

Fig. 4 Hypothetical pattern for 3-arm star molecule assemblies containing green di-gonal 'lenses'.

While topologically acceptable, these disordered patterns are unlikely to be found in ABC star systems containing monodisperse molecules, since the latter prefer roughly equivalent domains for each arm in all molecules. Further, these patterns have very different red and blue domains; a situation that is inconsistent with the equal red and blue arms. However, both domains can be made equivalent if the necklaces are opened to form infinite strings, giving 3D patterns of red and blue lamellae, decorated by green cylinders. Further, ordered placement of the green digons leads to equivalent red and blue domain shapes (fig. 6(a)). Since the green domains are very different to the red and blue, these patterns would be expected to form only for small x values in a $1:1:x$ star molecule. Our MD simulations have produced 'smeared' lamellar patterns, with the green domains mixed uniformly with the red and blue domains, rather than these demixed patterns. That result is likely to depend only on the relative strength of attractive interactions within the green beads, compared with repulsive interactions between green and other bead colours. Further, our coarse-grained simulations assign only one or two beads to the green arms, so arm folding to allow di-gon formation is unlikely. Indeed, this 'decorated lamellar' pattern has been reported in miktoarm copolymer Monte Carlo simulations [13].

Consider next the possibility of 4-sided green domains. A number of planar tessellations are possible, corresponding to positive (and even) integer solutions to eq. 7. If we demand that $n_R = n_B$, the $[8.8.4]$ tiling results, observed in our simulations for $x = \frac{1}{2}$. If the green domains are hexagons, both red and blue domains are also hexagonal (the $[6.6.6]$ tiling), also observed for $x = 1$. If the green domains are polygons whose order exceeds 6, corresponding to $x \geq 1$, eq. 7 demands that the blue and red domains can only be combinations of 2-, 4- and 6-gons, since the average polygonal size must be 6. In contrast to larger miktoarm copolymers (discussed above), 2-gons are less likely to form in polyphiles than larger polygons. We therefore consider mixtures of 4- and 6-gons only. A

large number of tilings are possible, which we construct with a generic algorithm, that yields – among others – all of the relevant tilings found in the simulations.

5 Spoke algorithm

To generate suitable tiling topologies, we decorate 2D hexagonal arrays of discs with spokes along the three equivalent directions between closest neighbors. The simplest patterns have equivalent decorations, denoted $[s_1,s_2,s_3]$, for example the $[1,1,1]$ case gives the $[6.6.6]$ tiling, shown in Fig. 5 along with two other examples. Also, in Fig. 6 two lamellar patterns are shown corresponding to the [1,0,0] and [2,0,0] decorations. We use this spoke algorithm to generate tiling topologies that obey the constraints for possible tilings of three-arm star assemblies deduced above.

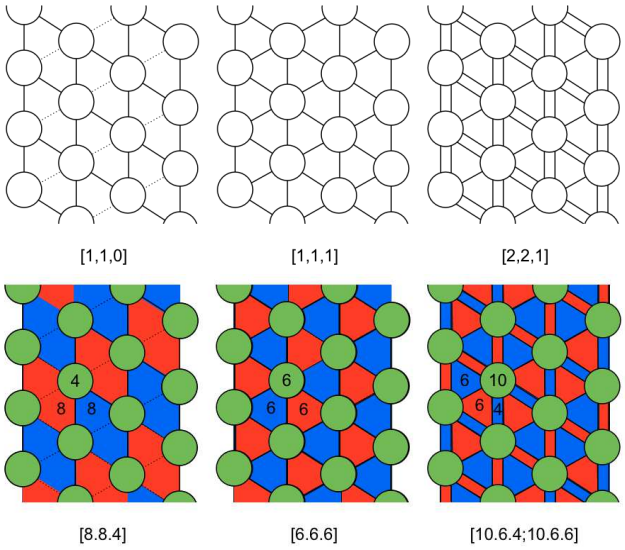

Fig. 5 A hexagonal array of discs, with nearest neighbours along three distinct axes (dashed lines). Generic 2D patterns are formed by linking discs along these three axes with single-, double-, ... spokes (top row), leading to different three-colored tilings (bottom row). Full list of patterns generated are shown in Table 1.

An additional suite of topologically inhomogeneous patterns are generated if we relax the requirement that all discs be equally decorated by spokes. Thus, for example, two distinct spoke decoration in alternating columns of discs – that we denote by the symbol $[2,2,1;2,1,1]$ – results in the $[8.6.4;10.6.4]$ tiling, observed in one simulation and illustrated in Figure 8(n)).

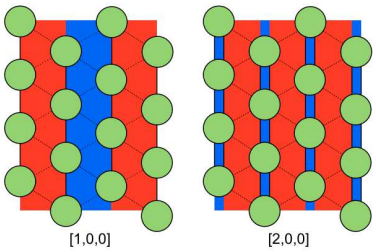

Fig. 6 Lamellar patterns formed by decorating the discs of fig. 5 with spoke arrangements, *cf.* Table 1. The patterns correspond to (left) decorated lamellae ($[1,0,0]$), (right) alternating lamellae pattern ($[2,0,0]$).

6 Relative energies of various patterns

The spoke algorithm can be used to generate an unlimited number of tilings. In order to decide the patterns likely to appear in condensed materials made up of star molecules, some ranking of the relative energies of various patterns is therefore needed. A simple working hypothesis that we test here is that the 2D tiling patterns found in simulations are those with smaller interfacial (suitably normalised) lengths between distinct polygonal domains. That length is proportional to the surface tension acting to miminise the area of domain walls in the columnar domains formed by extruding the tilings along a third perpendicular axis[26].

We therefore compare the relative stability of distinct topologies patterns subject only to an interfacial energy contribution for each pattern, that scales with $\frac{\lambda_{uc}}{A_{uc}}$, where λ_{uc} is the total length of the edges in a given pattern per unit cell and A_{uc} is the unit cell area. We can reduce the interfacial energy (dependent on the area of the domain walls) to an energy per length of the 2D cross-section of the prismatic patterns by noting that the area scales as λb, where b is the thickness of a slice of the pattern, equal to the molecule centre-to-centre spacing between adjacent molecules lining the three-fold branch lines (normal to the 2D tiling patterns, located at the vertices of the tilings). Each star-polyphile molecule of composition $1:1:x$ occupies a volume $(2+x)b$ and there are N molecules per unit cell, where N denotes the number of vertices of the tiling within a unit cell. The energy per molecule is then

$$E_{mol} \sim \frac{\lambda_{uc} b}{N}$$

and λ_{uc} is the total edge-length of the tiling within a unit cell, scaled to contain red and blue domains of unit volume. The volume of the unit cell is $(2+x)Nb$, giving a 2D cross-sectional area of

$$A_{uc} = N(2+x),$$

equal to the area of the unit cell of the 2D tiling pattern. The tiling edge length depends on the unit cell area A_{uc}, and varies as

$$\lambda_{uc} = \lambda_0 (\frac{A_{uc}}{A_0})^{1/2}$$

where λ_0 and A_0 are units of length and area respectively.

Therefore

$$\lambda_{uc} \sim \lambda_0 \frac{(N(2+x))^{1/2}}{A_0^{1/2}}$$

giving

$$E_{mol} \sim \frac{\lambda_0 (2+x)^{1/2} b}{(NA_0)^{1/2}}, \quad (8)$$

or, per unit volume,

$$E_v \sim \frac{\lambda_0}{(NA_0(2+x))^{1/2}}, \quad (9)$$

We have argued in a related analysis[26] that the relative interfacial energies of tricontinuous patterns for 'balanced' 3-arm star polyphiles (with composition $1:1:1$) scale as:

$$E_s \sim \varepsilon^{-1/2} \quad (10)$$

where the parameter $\varepsilon := \frac{V\Lambda}{\Sigma^2}$ is a dimensionless measure of the interfacial geometry and V, Λ and Σ denote the volume, triple-line length and interfacial area per unit cell. That scaling can be expressed in terms of the structural parameters for the prismatic patterns that result from 2D tilings considered here as follows. The triple-line length, $\Lambda = Nb$, the cell volume $V = Ab$ and the area $\Sigma = \lambda b$, so that

$$\varepsilon = \frac{AN}{\lambda^2} \quad (11)$$

and eq. 9 can be rewritten:

$$E_v \sim ((2+x)\varepsilon)^{-1/2} \quad (12)$$

reconciling eqs. 9,10.

Equation 12 can be used to estimate the relative interfacial energies per molecule for the suite of 2D tilings listed in Table 1, via the geometric parameters ε and x. If we assume that the free energy of these star molecular assemblies depends only on the surface tension, we can deduce optimal geometries for each tiling pattern as a function of x by relaxing the various pattern topologies to minimize the value of λ. It is well known - though only recently proven[40] - that the relaxed geometry for the $[6.6.6]$ pattern and $x = 1$ is the hexagonal honeycomb, the stable configuration of a two-dimensional froth with equal bubbles. This pattern is identical to the barycentric embedding of $[6.6.6]$ (drawn in Fig. S2). This "balanced" case ($x = 1$) is, to the best of our knowledge, the only one for which the optimal pattern, with minimal scaled edge length separating bubbles (our ε) is known. Extensions of that to three-coloured patterns with composition $1:1:x$ is a simple generalization of the problem to unequal cells. As famously recognized by Lord Kelvin, when exploring the three-dimensional analogue of our $x = 1$ problem, "the problem is solved in foam"[41], due to the surface tension of soap films. Our simpler problem, whose solutions are prisms, are solved in dry two-dimensional bubble rafts, where the bubble areas are tuned to $1:1:x$ fractions about each vertex.

A convenient realization of various topologies realized by the spoke algorithm are the barycentric embeddings, (where each vertex lies at the barycenter of its neighbouring vertices, see Figure S2). We can build those embeddings using the *Systre* software of Delgado Friedrichs[42,43]. These embeddings realize without exception the most symmetric possible geometry for a given topology[43], whose symmetry is characterised by the 2D orbifold, notated using Conway's notation[44]. Force balance between edges of 2D dry foams demands that edges coincident to a vertex invariably subtend angles of $\frac{2\pi}{3}$ with each other at equilibrium. Among the patterns generated by our spoke algorithm, only the $[6.6.6]$ case fulfils this condition without some geometric distortion of the straight-edge barycentric embeddings. Generic patterns adopt this optimal geometry by curving edges to achieve the required angles.

7 *Surface Evolver* calculations

Given the complexity of Hales' proof of the honeycomb conjecture, we have resorted to numerical software to determine relaxed geometries with minimal edge lengths for the spoke patterns as a function of the composition x. We use the freely available *Surface Evolver* software[45], which is ideally suited to estimate optimal, relaxed geometries for films (and in our case one-dimensional "threads") under surface tension.

First, we build tiling patterns whose topologies are those formed by our spoke algorithm. As shown in Figure 7 each pattern is optimized starting from an arbitrary initial state fulfilling the relevant topological requirement, given by the complement of vertices and edges per translational unit cell in their barycentric counterparts. This allows us to relax the patterns using the string-model implemented in *Surface Evolver* (version 2.70a). In particular, all patterns are relaxed in a (flat) torus, enforcing translational symmetry via periodic boundary conditions. The dimensions of the torus, and the related 2D unit cell are varied to determine the global minima of edge lengths for a given tiling pattern and x. Two parameters determine those dimensions: the ratio between the two lattice vectors of the unit cell, χ, and the angle between those vectors, θ. By thoroughly sweeping ranges of θ and χ values and minimizing the emerging patterns, we can estimate the optimal unit cell for a given x as well as the associated interfacial en-

Table 1 List of planar patterns formed by decorating the hexagonal array of discs of Fig. 5 with various spoke multiplicities along the three directions linking nearest discs. Patterns formed with s_1, s_2 and s_3 parallel spokes along the three directions are denoted in the Table $[s_1,s_2,s_3]$. Increasing x results in patterns with higher spoke numbers (s_i). The tabulated space groups and number of symmetrically distinct vertices N_v (contained within the shaded asymmetric domain) refer to the symmetries of 3-coloured tilings.

Pattern	$[s_1,s_2,s_3]$	*Figure*	*2D symmetry - uncolored*	*2D symmetry - colored*	*3D symmetry - colored*	N_v
$[\infty,\infty.2]$	$[1,0,0]$	6(a)	$*2222$	$*\times$	*cm*	1
[8.8.4]	$[1,1,0]$	8(b)	$*244$	$*244$	p4mm	1
[6.6.6]	$[1,1,1]$	8(c)	$*236$	$*333$	p3m1	1
[8.6.4;8.8.6]	$[2,1,0]$	8(k)	$*2222$	$*2222$	*p2mm*	3
[8.4.4;8.8.8]	$[3,1,0]$	8(l)	$*2222$	$2*22$	*c2mm*	4
[8.6.4;8.6.6]	$[2,1,1]$	8(d)	$*2222$	$*2222$	p2mm	4
[8.6.4;10.6.4]	$[2,2,1;2,1,1]$	8(n)	2222	2222	p2	18
[10.4.4;10.6.4;10.6.6]	$[3,1,1]$	8(m)	$*2222$	$*\times$	*cm*	5
[10.6.4;10.6.6]	$[2,2,1]$	8(e)	$2*22$	$22*$	*p2mg*	5
[12.6.6;12.6.4;12.4.4]	$[3,2,1]$	8(f)	2222	2222	*p2*	10
[12.6.4]	$[2,2,2]$	8(g)	$*236$	$*236$	p6mm	1
[14.6.4;14.4.4]	$[3,2,2]$	8(h)	$2*22$	$22*$	p2mg	7
[16.6.4;16.4.4]	$[3,3,2]$	8(i)	$*2222$	$*2222$	*p2mm*	8
[18.6.4;18.4.4]	$[3,3,3]$	8(j)	$*236$	$*333$	*p3m1*	*3*
[12**z**.6.4;12**z**.4.4]	$[2\mathbf{z},2\mathbf{z},2\mathbf{z}]$		$*236$	$*236$	*p6mm*	**z**
$[(12\mathbf{z}+6).6.4;$ $\cdots(12\mathbf{z}+6).4.4]$	$[2\mathbf{z}+1,2\mathbf{z}+1,$ $\cdots 2\mathbf{z}+1]$		$*236$	$*333$	*p3m1*	$2\mathbf{z}+1$
[4.4.∞]	$[2,0,0]$	6(b)	$*2222$	$*2222$	*p2mm*	1

ergy. For more details, see the Supporting Information where an example of the resulting energy landscape can be found.

We have used batch scripts in *Surface Evolver* to estimate the relaxed configurations of vertices and unit cell parameters for the suite of tiling patterns in Table 1 resulting from the spoke algorithm. All relaxed embeddings found by *Surface Evolver* were found to exhibit the same "maximal" symmetry realised by the unrelaxed barycentric embeddings. In general however – excepting the [6.6.6] case – the edges curve to minimise their edge length, as discussed above. Those relaxed patterns allow us to estimate the energies per unit volume for all tilings, using equation 12. The results are shown in Figure 9.

The *Surface Evolver* results suggest a rich sequence of optimal 3-colored foam-like tilings from the suite generated by the spoke algorithm and listed in Table 1 – with minimal edge length – and 2D bubble area fractions (or prism volume fractions) $1:1:x$. The normalised interfacial energies per volume (eq. 12) are plotted for the various tilings in Fig. 9. In order of increasing x we find the following 2D tilings to be optimal for $x<3$: $[8.8.4]\cdot[6.6.6]\cdot[10.6.4;10.6.6]\cdot[12.6.4]\cdot[14.6.4;14.4.4]\cdot[16.6.4;16.4.4]\cdot[18.6.4;18.4.4]$.

We estimate an upper bound for the energies of tiling patterns for larger x values as follows. Two infinite sequences of tilings are possible, with topologies [12**z**.6.4;12**z**.4.4] and $[(12\mathbf{z}+6).6.4;(12\mathbf{z}+6).4.4]$ where **z** is an integer and 2D symmetries corresponding to the orbifolds $*236$ and $*333$ re-

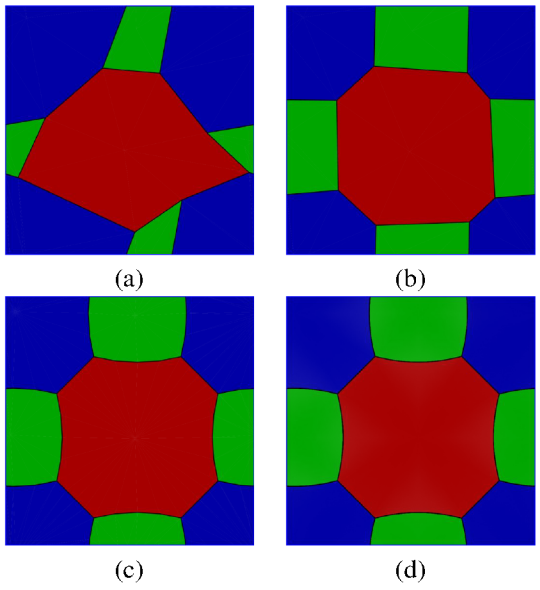

Fig. 7 Relaxation of the [8.8.4] tiling pattern using *Surface Evolver*. From an arbitrary initial configuration of vertices within the unit cell, (a), the pattern is subjected to a number of optimization steps and refinement routines, resulting in patterns such as (b) and (c), until an estimate of the relaxed pattern is obtained, (d). In this case, the pattern corresponds to the setting $x=0.8$, $\chi=1$, and $\theta=\pi/2$. The script responsible for the generation of this pattern is available in the Supporting Information.

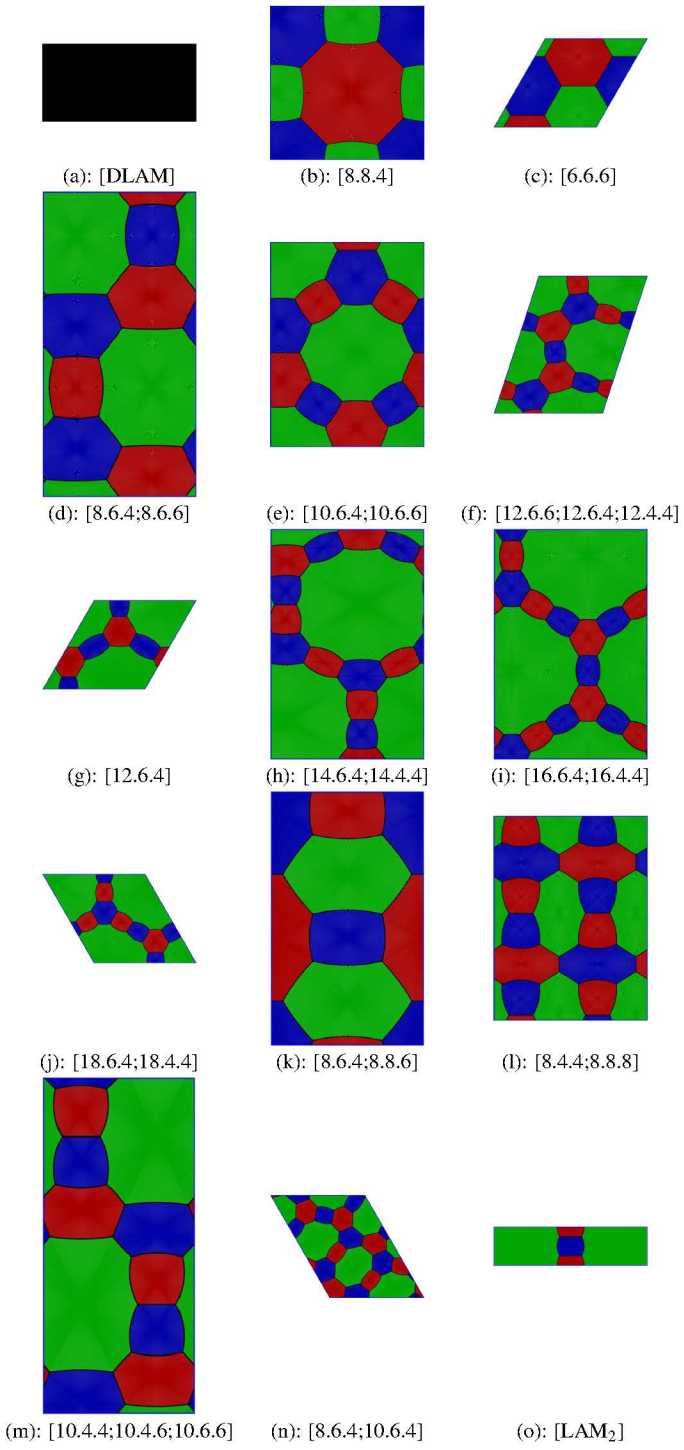

Fig. 8 Examples of relaxed patterns derived using *Surface Evolver* for selected values of χ, θ and x. The shown patch of the pattern corresponds to the region investigated by *Surface Evolver*, which is exactly the unit cell.

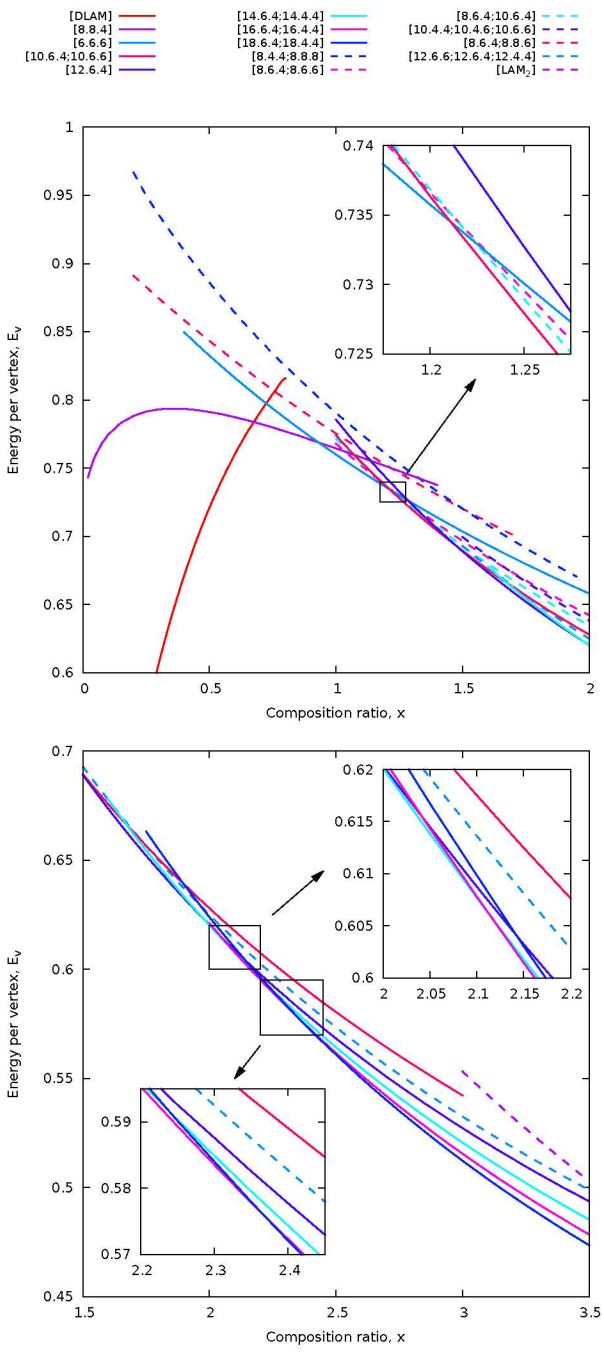

Fig. 9 The energy per vertex in the relaxed patterns as a function of x. The solid lines represents patterns that are realised in the phase diagram, whereas the dashed lines are topologies unable to compete energy-wise.

spectively. We will restrict our analysis to the latter case, but similar arguments apply to both series of patterns. The number of vertices within the orbifold, N, depends on $\mathbf{z}$, via the equation $N = 2\mathbf{z}+1$. One example is the $[18.6.4;18.4.4]$ pattern (Figure 10(b)), formed when $\mathbf{z}=1$. We estimate the tiling edge lengths, λ, from those of the unrelaxed barycentric embeddings. Since relaxed patterns necessarily have smaller edge lengths, the resulting energies are upper bounds for these tilings. Figure 10(b) and its generalisations imply $\lambda = 2+\frac{5\mathbf{z}}{2}$. The area of a single $*333$ domain depends on the side-length of the triangle, which contains $2\mathbf{z}$ unit edges and 2 in-circle radii of the unit hexagon ($\frac{\sqrt{3}}{2}$), forming an equilateral triangle of area $\frac{\sqrt{3}}{4}(2\mathbf{z}+\sqrt{3})^2$. It follows that

$$\varepsilon^{-1/2} = \frac{2+\frac{5\mathbf{z}}{2}}{\sqrt{(2\mathbf{z}+1)\frac{\sqrt{3}}{4}(2\mathbf{z}+\sqrt{3})^2}} = \frac{4+5\mathbf{z}}{3^{1/4}(\sqrt{3}+2\mathbf{z})\sqrt{1+2\mathbf{z}}}. \quad (13)$$

The composition of the green domain, x depends on $\mathbf{z}$ as follows. The $*333$ triangle contains $2\mathbf{z}.\frac{1}{2}$ unit squares and $2.\frac{1}{6}$ unit hexagons, split equally between red and blue domains, so that

$$x = \frac{\frac{\sqrt{3}}{4}(2\mathbf{z}+\sqrt{3})^2 - (\mathbf{z}+\frac{\sqrt{3}}{2})}{(\frac{\mathbf{z}}{2}+\frac{\sqrt{3}}{4})} = 1+2\sqrt{3}\mathbf{z}. \quad (14)$$

Thus, x and $\mathbf{z}$ are proportional so we can investigate the high x limit *via* $\mathbf{z}$, see below. The energy of the $[(12\mathbf{z}+6).6.4;(12\mathbf{z}+6).4.4]$ patterns then follows from eq. 12:

$$E_v \sim \frac{4+5\mathbf{z}}{3^{1/4}(\sqrt{3}+2\mathbf{z})\sqrt{1+2\mathbf{z}}}(3+2\sqrt{3}\mathbf{z})^{-1/2} \quad (15)$$

We will use this expression to explore optimal patterns in the limit of high x.

7.1 Comparison of 2D foams with hierarchical lamellae for large x

Recall that our simulations reveal striped lamellar patterns for large x, rather than prismatic patterns derived from the $[12\mathbf{z}.6.4;12\mathbf{z}.4.4]$ and $[(12\mathbf{z}+6).6.4;(12\mathbf{z}+6).4.4]$ families of tilings discussed above.

A crude upper bound for the energies for striped lamellar patterns follows by assuming that the width of red and blue stripes are equal and of width and height equal to 2 to normalize the red and blue domain areas (i.e. unit area per vertex), see Figure 10. The edge length, λ within an asymmetric domain is 3, $N=1$ and $A=a$. So,

$$\varepsilon^{-1/2} = \frac{3}{\sqrt{a}}.$$

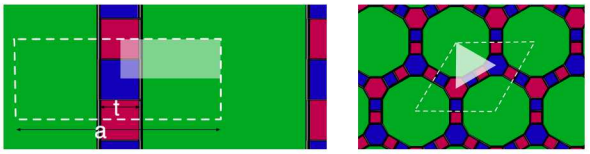

(a) (b)

Fig. 10 Unrelaxed barycentric embeddings of relevant high x patterns. (a) Striped lamellae (b) $[18.6.4;18.4.4]$, i.e. $[(12\mathbf{z}+6).6.4;(12\mathbf{z}+6).4.4]$ for $\mathbf{z}=1$. In (a) the labels a and t are the unit cell length and minority domain side lengths respectively with $t=2$, see text for details.

But the ratio of area of green to red (or blue) domains is $x = a-2$. So the energy scales as:

$$E_v \sim \frac{3}{(2+x)} \quad (16)$$

Equations 16 and 15 allow us to compare the interfacial energies of the striped lamellar and the $[(12\mathbf{z}+6).6.4;(12\mathbf{z}+6).4.4]$ patterns. Fig. 11 shows that the $[(12\mathbf{z}+6).6.4;(12\mathbf{z}+6).4.4]$ has slightly lower interfacial energy than the striped lamellar pattern, and the two energy curves remain almost parallel to very large x values.

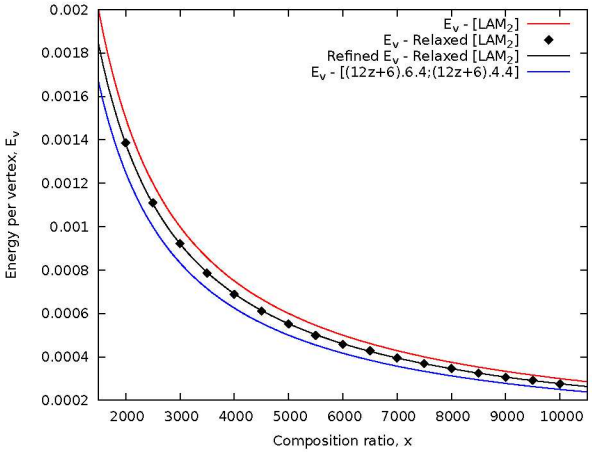

Fig. 11 The high-x limit of the $[\mathrm{LAM}_2]$ pattern and the $[(12\mathbf{z}+6).6.4;(12\mathbf{z}+6).4.4]$ pattern.

So the emergence of the striped lamellar pattern in the simulations can apparently not be ascribed to interfacial energy alone. To substantiate this, From equation 16, we see that:

$$\lim_{x\to\infty} E_{v,[LAM_2]} = \frac{3}{x} \quad (17)$$

and from equation 15, one can obtain that:

$$\lim_{x\to\infty} E_{v,[(12\mathbf{z}+6).6.4;(12\mathbf{z}+6).4.4]} = \frac{2.5}{x} \quad (18)$$

Eq. 21 and 22 are the upper bounds for the high x limit derived from the *unrelaxed* barycentric patterns, see Figure 10. We can sharpen the bound in Eq. 16 by relaxing the lamellar patterns in *Surface Evolver* and then calculating the energies per volume. The results are also plotted in Figure 11, and fit the function:

$$\lim_{x\to\infty} E_{v,[LAM_2],\text{Relaxed}} = \frac{2.76}{x} \quad (19)$$

Since the resulting values for the relaxed lamellar patterns are higher than the upper bound for the $[(12\mathbf{z}+6).6.4;(12\mathbf{z}+6).4.4]$ patterns, we conclude that the lamellar pattern is disfavoured compared with prismatic morphologies based on $[(12\mathbf{z}+6).6.4;(12\mathbf{z}+6).4.4]$ tilings of the type on the basis of interfacial energy alone. As stated above, the same arguments apply to the $[12\mathbf{z}+6.6.4;12\mathbf{z}+6.4.4]$ sequence which has the same limiting behavior.

Clearly, additional contributions to the free energy of these assemblies are relevant to molecular simulations. We explore differences between patterns expected on the basis of interfacial energy alone and those found in various simulations in more detail next.

8 Comparison of 2D foams with simulated morphologies

It is fruitful to collate phase sequences found from simulations of $1:1:x$ 3-arm star assemblies in addition to those reported in this paper, and to compare all of those data with the expected phase sequence determined on the basis of interfacial energy alone, reported above. We collect those results in Figure 12, where distinct studies occupy separate rows in the diagram; the studies are (from bottom to top): *Surface Evolver* calculations reported here, MD simulations from the present work, Monte Carlo simulations [13], DPD simulations [15,21] and SCFT calculations [18–20]. The SCFT results occupy two rows, corresponding to two distinct segregation levels: with $\chi N = 60$ and $\chi N = 30$ data [19,20] in the lower and upper rows respectively.

Comparison of the phase sequence displayed in the bottom row with those in higher rows reveals the importance of interfacial energy and related three-coloured foam-like patterns in explaining most – though not all – tiling patterns reported to date. [8.8.4], [6.6.6], [8.6.4;8.6.6], [10.6.4;10.6.6] and [12.6.4] patterns are realized in various simulations, in the same sequence of x values as that found from *Surface Evolver* calculations. However, their absolute location on the composition (x) axis is at increasingly lesser x values than predicted on the basis of interfacial energy alone as one progresses from lower to higher rows. We view this as an effect of chain configurational entropy as discussed in the following.

Note first that the relative contributions of chain configurational entropy to the free energy of the assemblies likely increases monotonically from bottom to top in the figure. The bottom row, deduced on the basis of interfacial energy alone, ignores all entropic effects. The row immediately above encodes patterns inferred from the MD simulations reported here, that involve short chains, subject to relatively hard potentials. The next higher row describes DPD and MC data resulting from simulated terpolymer assemblies with longer chains, interacting via softer potential. The topmost two rows describe simulated phase sequences for the SCFT calculations that model polymers as infinitely long chains. In broad terms then, the lower sequences are relevant to small molecules, such as three-arm star polyphiles while upper sequences are germane to high molecular weight miktoarm copolymers. Differences in those sequences therefore reflect the increasing contributions of chain configurational entropy.

The effect of chain entropy on the stability of various morphologies is difficult to quantify, however entropically-favourable patterns are likely to be qualitatively coupled to their geometry as follows. The presence of more than one distinct domain geometry for a single A, B or C moiety of the ABC molecules – found for example in locally inhomogeneous tilings with more than one distinct vertex – is likely disfavoured on entropic grounds. Thus, a very simple measure of the configurational entropy is the degree of packing homogeneity, given by the number of symmetrically distinct vertices (N) in the barycentric embedding of the coloured tiling, since that is also the number of different domain shapes the ABC molecules must adopt to form the tiling. A single domain shape results only when $s_1 = s_2 = s_3$, which form trigonal or hexagonal patterns. The number of distinct vertices is listed in Table 1.

While this measure is appealing in its simplicity, it can not be the full story. Indeed, some of the tiling patterns contain few topologically distinct vertices, but nevertheless display large differences in polygon types for a single colour, also likely to be disfavoured on entropic grounds. For example, among all the patterns considered here, $[8.6.4;8.8.6]$ and $[8.4.4;8.8.8]$ exhibit the largest inhomogeneities in red and blue domain shapes (and area fractions, corresponding to local compositions), due to the presence of both squares and octagons for these colors. In contrast, the $[6.6.6]$ pattern has no such inhomogeneities. (For this reason we have not analysed in detail related patterns resulting from the spoke algorithm. For example, the [8.6.4;8.8.4;12.6.4;12.8.4] tiling considered previously [18] (spoke pattern [2,2,2;0,2,2]) but later dismissed as an equilibrium structure, even when lifting the $1:1:x$ constraint [20], is unlikely to be an entropically favoured structure).

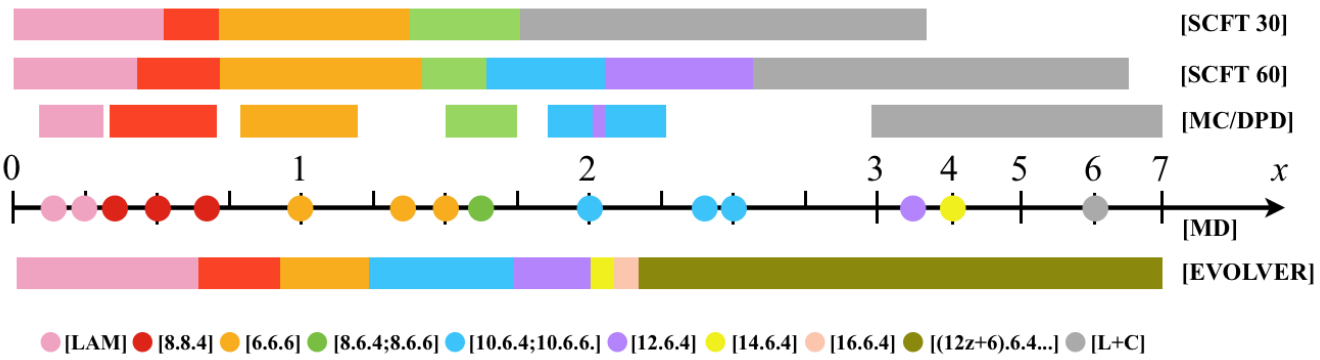

Fig. 12 Comparison of phase diagrams derived from *Surface Evolver* calculations and MD simulations (this work) and previous calculations using SCFT [19,20], MC [13] and DPD [15,21]. The SCFT results are divided into two parts at high x representing different segregation levels, $\chi N = 30$ in upper half, $\chi N = 60$ in lower half, see text for details. In general the importance of chain entropy increases from bottom to top.

The observation that the [8.6.4;8.6.6] tiling pattern is observed in preference to the [6.6.6] pattern in an increasing x-range as we move upwards in Figure 12 is also consistent with the notion of increasing importance of chain packing entropy from bottom to top. Here an additional effect of chain entropy is likely at work: the entropic cost of anisotropic domain shapes (which can only be realised at the cost of reduced chain entropy). Though the [6.6.6] tiling is topologically homogenous, with a single vertex type, it is less favoured in terms of chain packing frustration [46], particularly for the majority domain as $x > 1$. Allowing the majority domain to relax into a octagonal shape (more round) becomes increasingly important for longer chains, favouring the [8.6.4;8.6.6] tiling pattern over the [6.6.6] pattern; a very different situation from that found for '2-coloured' interfacial energies, such as soap froths in air, where the hexagonal honeycomb is the most stable form.

Figure 12 reveals an increasing compositional range for the striped lamellae from bottom to top. Recall that in the limit of large x, this hierarchical lamellar morphology [L+C] is *never* favoured on the basis of interfacial energy alone, since higher order tiling patterns have less interfacial area per volume. Clearly, the appearance of this pattern is a result of entropic stabilization, as discussed briefly by others [19]. The ever-broadening compositional window for the [L+C] pattern, appearing at lower and lower x as we move up rows in Figure 12 is therefore very likely to be due to the increasing importance of chain stretching entropy. This phase is the most striking violation of the phase sequence expected on the basis of interfacial energy alone. For smaller values of x, differences between the sequence predicted from foam-like energy alone, and simulated patterns are less dramatic, pointing to the importance of interfacial energy for these molecular compositions. Nevertheless, some discrepancies between the foam model and observed phase sequences are seen.

We note that among the tilings formed in our MD simulations, two are not formed in the presence of interfacial energy alone, namely the [8.6.4;8.6.6] and [8.6.4;10.6.4] patterns. However, as shown in the inset of Figure 9(top), the interfacial energies per volume for these patterns are very close to the most favoured patterns, *viz.* the [6.6.6] and [10.6.4;10.6.6] patterns, at x = 1.22, in contrast to all the other patterns. It is therefore reasonable to infer that precisely the occurrence of these two tiling patterns in the simulations is due in large part (though not *in toto*) to their low interfacial energies. Alternatively, additional mesophases which are entropically disfavored, but favored on interfacial energetic grounds, are likely to be further stabilized by, for example, adding (monomer) solvent to pure polyphile mixtures, so that the solvent is preferentially partitioned to entropically inaccessible locations for the polyphile chains. In fact, our results here indicates that a richer polymorphic behavior is expected in polyphilic star self-assemblies compared to miktoarm melts, since the chain stretching entropy clearly destabilizes several candidate structures which are optimal in terms of interfacial energy.

9 Self-assembly of $1 : x : y$ polyphiles: a [3.3.4.3.4] tiling

Similar simulations on more general 3-arm polyphile compositions reveal a wide spectrum of chain compositions beyond those with $1 : 1 : x$ fractions. We can increase the complexity of the tiling patterns further by allowing all of the 3 arms to have different lengths, so that the polyphile has schematic composition $1 : x : y$. Evidently, the resulting phase space is far larger than that of the $1 : 1 : x$ family discussed above, and our findings remain scattered. We mention here just one result,

that has interesting implications discussed below.

In Figure 13 we see the result from simulating a star with 2,4 and 6 beads respectively, i.e. an arm length ratio of 1:2:3. The resulting pattern contains 4-, 6- and 8-gons containing the lesser arms and has symbol [10.6.4;10.8.4]. Alternatively, it can be described by a superimposed [3.3.4.3.4] tiling, where vertices describe centres of the 10-gons only. The same pattern was found to be stable with the same composition ratio in SCFT[20]. This tiling is commonly known as the σ phase in the Frank-Kasper complex crystalline alloy family, and is a crystalline approximant to the 2D dodecagonal quasicrystal[47]. The presence of this crystalline approximant lends some weight to the possibility that these $1:x:y$ polyphiles may also form quasi-crystals, by e.g. a slight modification of the x,y values. Indeed, 2D decagonal quasi-crystals have been detected in miktoarm copolymeric systems, with the addition of homopolymer to the miktoarm copolymer blend[47]. The possibility of forming a polyphilic quasicrystal in experimental systems is therefore real, and may be achieved by gradual tuning of the x,y parameters. This can be done in actual polyphilic solutions by selective solvent swelling.

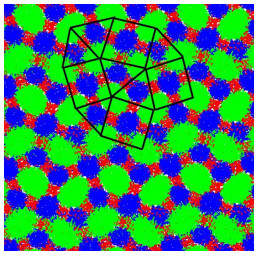

Fig. 13 A [10.6.4;10.8.4] tiling with symmetry $4*2$ from a simulation of a 1:2:3 arm length ratio star ((2,4,6) beads). The tiling can also be described by a [3.3.4.3.4] tiling pattern superimposed.

10 Generalising to four-arm polyphile prismatic patterns

The topological analysis above admits extension to star-shaped polyphilic assemblies with four mutually immiscible arms. In that case, degree-four tilings are required and the 4-colouring requirement constrains the polygons to contain an even number of sides, as for the 3-coloured patterns. Euler's relation for degree-4 tilings implies that the average polygonal size must be equal to four; indeed, the simplest pattern, accessible to a 4-arm polyphile with composition $1:1:1:1$ is the [4.4.4.4] (square) planar tessellation. However, in three dimensions the equilibrium morphology is actually a cellular packing, conjectured to be the Kelvin foam[48]. Nevertheless, since the average polygonal size is 4, prismatic patterns whose sections are 2D planar tessellations with larger polygons than 4-gons necessarily also contain 2-gons. Our simulations of 3-arm star polyphiles suggest that the presence of these lens-shaped di-gonal domains is unlikely for reasons discussed above. We may therefore conclude that 4-arm polyphilic systems do not display the wealth of 2D tiling patterns found in the 3-arm case; at least for the interaction parameters (and coarse-grained approximations) invoked to date. It is possible, however, that tuning of the simulation details may allow the formation of lens-shaped domains. In those cases, a wealth of 2D patterns again appear, that are formed from the 3-arm 2D tilings by insertion of di-gons as follows. We replace the spoke decorations used to form the 2D tilings in the 3-arm system by curved 'twinned' spokes, as illustrated in fig. 14.

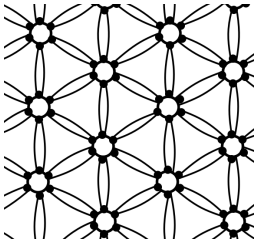

Fig. 14 A decorated $[1,1,1]$ pattern, with pairs of curved 'twin' spokes along each direction, that meet at either hub, forming 2-sided lens-shaped regions. The discs contain 6 degree-four vertices, and the resulting pattern has topology [6.6.6.2].

Every 3-arm tiling formed via the algorithm described above can be morphed into a pattern that is consistent with a 4-arm star polyphile assembly by this twinning operation, forming lenses of the 4th arm in place of edges of the original 3-arm tiling. A simple example is the degree-4 [8.2.8.4] pattern shown in fig. 15.

11 Conclusions

This paper has been motivated in part by the question of differences in phase behavior between longer chain terpolymers, and short-chained 3-arm star polyphiles. Our simulations – most apposite to shorter-chained star molecules, such as star polyphiles, suggest a rich polymorphism is possible beyond the single [12.6.4] hexagonal mesophase already found experimentally[27]. In principle, additional mesophases are likely to form by adding solvents that selectively dissolve in just one of the three chain moieties. We have detected a number of novel 2D and 3D crystalline mesophases, one of which hints at the presence of quasi-crystallinity in these systems, a phenomenon that has already been observed in miktoarm copolymeric melts. Most strikingly, we find that the range of mesophases is richer in 3-arm star molecular assemblies whose free energy is not dominated by chain entropy, such

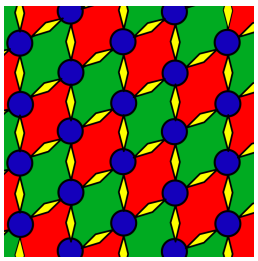

Fig. 15 A planar [8.2.8.4] tessellation with symmetry ∗2222 that is consistent with the molecular architecture of 4-arm star polyphiles. The pattern is formed from the [8.8.4] pattern of fig. 6(b) by insertion of (yellow) lenses (di-gons) in place of the spokes used to create the (3-arm) [8.8.4] pattern. *All* planar tessellations that are possible sections of 4-arm star polyphile assemblies contain these lenses, apart from the [4.4.4.4] tiling, which is the 4-arm analogue of the [6.6.6] tiling found in 3-arm polyphiles with composition 1 : 1 : 1.

as oligomeric star polyphiles. This finding is in line with the analogous situation for 2-arm systems, where amphiphilic assemblies often display more than the single bicontinuous morphology typically found in diblock copolymer melts, namely the Gyroid. In amphiphiles it is not uncommon to find both the P, D and G in a single system as a function of water content[49]. In broad terms, we conclude that the complex prismatic phases related to 2D tiling patterns of the plane form in response to the interfacial energy of star assemblies, regardless of their molecular weights. Detailed exploration of the relative interfacial energies of a variety of patterns generated by a spoke algorithm introduced here offers a useful route to topologically feasible patterns for 3- and 4-arm star polyphiles, as well as higher molecular weight analogues, such as miktoarm star copolymers.

References

1 S. Sioula, N. Hadjichristidis and E. Thomas, *Macromolecules*, 1998, **31**, 8429–8432.
2 S. Sioula, N. Hadjichristidis and E. Thomas, *Macromolecules*, 1998, **31**, 5272–5277.
3 A. Zioga, S. Sioula and N. Hadjichristidis, *Macromolecular Symposia*, 2000, **157**, 239–249.
4 K. Yamauchi, S. Akasaka, H. Hasegawa, H. Iatrou and N. Hadjichristidis, *Macromolecules*, 2005, **38**, 8022–8027.
5 A. Takano, W. Kawashima, S. Wada, K. Hayashida, S. Sato, S. Kawahara, Y. Isono, M. Makihara, N. Tanaka, D. Kawaguchi and Y. Matsushita, *J. Polym. Sci. B*, 2007, **45**, 2277–2283.
6 A. Takano, S. Wada, S. Sato, T. Araki, K. Hirahara, T. Kazama, S. Kawahara, Y. Isono, A. Ohno, N. Tanaka and Y. Matsushita, *Macromolecules*, 2004, **37**, 9941–9946.
7 K. Hayashida, W. Kawashima, A. Takano, Y. Shinohara, Y. Amemiya, Y. Nozue and Y. Matsushita, *Macromolecules*, 2006, **39**, 4869–4872.
8 K. Yamauchi, K. Takahashi, H. Hasegawa, H. Iatrou, N. Hadjichristidis, T. Kaneko, Y. Nishikawa, H. Jinnai, T. Matsui, H. Nishioka, M. Shimizu and H. Fukukawa, *Macromolecules*, 2003, **36**, 6962–6966.
9 K. Hayashida, A. Takano, S. Arai, Y. Shinohara, Y. Amemiya and Y. Matsushita, *Macromolecules*, 2006, **39**, 9402–9408.
10 K. Hayashida, N. Saito, S. Arai, A. Takano, N. Tanaka and Y. Matsushita, *Macromolecules*, 2007, **40**, 3695–3699.
11 A. Takano, W. Kawashima, A. Noro, Y. Isono, N. Tanaka, T. Dotera and Y. Matsushita, *Journal of polymer science part B - polymer physics*, 2005, **43**, 2427–2432.
12 T. Dotera and A. Hatano, *J. Chem. Phys.*, 1996, **105**, 8413.
13 T. Gemma, A. Hatano and T. Dotera, *Macromolecules*, 2002, **35**, 3225–3227.
14 Y. Bohbot-Raviv and Z.-G. Wang, *Phys. Rev. Lett.*, 2000, **85**, 3428–3431.
15 C.-I. Huang, H.-K. Fang and C.-H. Lin, *Phys. Rev. E*, 2008, **77**, 031804.
16 Y. Matsushita, A. Takano, K. Hayashida, T. Asari and A. Noro, *Polymer*, 2009, **50**, 2191–2203.
17 P. Tang, F. Qiu, H. Zhang and Y. Yang, *Journal of Physical Chemistry B*, 2004, **108**, 8434–8438.
18 G. Zhang, F. Qiu, H. Zhang, Y. Yang and A. Shi, *Macromolecules*, 2010, **43**, 2981–2989.
19 W. Li, Y. Xu, G. Zhang, F. Qiu, Y. Yang and A. Shi, *J. Chem. Phys.*, 2010, **133**, 064904.
20 W. Xu, K. Jiang, P. Zhang and A. Shi, *J. Phys. Chem. B*, 2013, **117**, 52965305.
21 J. J. K. Kirkensgaard, *Phys. Rev. E*, 2012, **85**, 031802.
22 J. J. K. Kirkensgaard, *Interface Focus*, 2012, **2**, 602–607.
23 J. Kirkensgaard, M. Evans, L. de Campo and S. Hyde, *Proc. Natl. Acad. Sci. USA*, 2014, **111**, 1271–1276.
24 J. J. K. Kirkensgaard, *Soft Matter*, 2011, **7**, 10756–10762.
25 J. J. K. Kirkensgaard and S. Hyde, *Phys. Chem. Chem. Phys.*, 2009, **11**, 2016–2022.
26 S. T. Hyde, L. de Campo and C. Oguey, *Soft Matter*, 2009, **5**, 2782–2794.
27 L. de Campo, T. Varslot, M. Moghaddam, J. Kirkensgaard, K. Mortensen and S. Hyde, *Phys. Chem. Chem. Phys.*, 2011, **13**, 3139–3152.
28 Y. Lin, Y. Ou, A. Cheetham and H. Cui, *Macro Letters*, 2013, **2**, 1088–1094.
29 K. Ueda, T. Dotera and T. Gemma, *Physical Review B*, 2007, **75**, 195122.
30 T. Dotera and T. Gemma, *Phil. Mag.*, 2006, **86**, 1085–109.
31 J. J. K. Kirkensgaard, *Soft Matter*, 2010, **6**, 6102–6108.
32 A. Crane, F. Martinez-Veracoechea, F. Escobedo and E. Müller, *Soft Matter*, 2008, **4**, 1820–1829.
33 A. Crane and E. Müller, *Faraday Discuss.*, 2010, **144**, 187–202.
34 I. R. Cooke, K. Kremer and M. Deserno, *Phys. Rev. E*, 2005, **72**, 011506.
35 I. R. Cooke and M. Deserno, *J. Chem. Phys.*, 2005, **123**, 224710.
36 S. Midtgaard, M. Pedersen, J. Kirkensgaard, K. Sørensen, K. Mortensen, K. Jensen and L. Arleth, *Soft Matter*, 2014, **10**, 738.
37 H. J. Limbach, A. Arnold, B. A. Mann and C. Holm, *Comp. Phys. Comm.*, 2006, **174**, 704–727.
38 W. Humphrey, A. Dalke and K. Schulten, *Journal of Molecular Graphics*, 1996, **14**, 33–38.
39 S. T. Hyde, *Handbook of Applied Surface and Colloid Chemistry*, John Wiley and Sons, Ltd, 2001, ch. 16.
40 T. C. Hales, *Discr. Comput. Geom.*, 2001, **25**, 1–22.
41 Lord Kelvin (Sir William Thomson), *Philosophical Magazine*, 1887, **24**, 503.
42 O. Delgado-Friedrichs, *The Gavrog Project*, 2008, Available at http://www.gavrog.org/.
43 O. Delgado-Friedrichs and M. O'Keeffe, *Acta Cryst. A*, 2003, **59**, 351–360.
44 *The Symmetry of Things*, ed. J. H. Conway, H. Burgiel and C. Goodman-Strauss, AK Peters Ltd., 2008.

45 K. Brakke, Available at http://www.susqu.edu/brakke/evolver/evolver.html.
46 M. Fischer, L. de Campo, J. Kirkensgaard, S. Hyde and G. Schröder-Turk, *In review*, 2014.
47 K. Hayashida, T. Dotera, A. Takano and Y. Matsushita, *Phys. Rev. Lett.*, 2007, **98**, 195502.
48 T. Dotera, *Phys. Rev. Letters*, 1999, **82**, 105.
49 C. Kulkarni, T.-Y. Tang, A. Seddon, J. Seddon, O. Cesa and R. Templer, *Soft Matter*, 2010, **6**, 3191–3194.